

# Statistical Studies of Giant Pulse Emission from the Crab Pulsar

walid.a.majid@jpl.nasa.gov

Walid A. Majid<sup>1</sup>, Charles J. Naudet<sup>1</sup>, Stephen T. Lowe<sup>1</sup>, Thomas B. H. Kuiper<sup>1</sup>

## ABSTRACT

We have observed the Crab pulsar with the Deep Space Network (DSN) Goldstone 70 m antenna at 1664 MHz during three observing epochs for a total of 4 hours. Our data analysis has detected more than 2500 giant pulses, with flux densities ranging from 0.1 kJy to 150 kJy and pulse widths from 125 ns (limited by our bandwidth) to as long as 100  $\mu$ s, with median power amplitudes and widths of 1 kJy and 2  $\mu$ s respectively. The most energetic pulses in our sample have energy fluxes of approximately 100 kJy- $\mu$ s. We have used this large sample to investigate a number of giant-pulse emission properties in the Crab pulsar, including correlations among pulse flux density, width, energy flux, phase and time of arrival. We present a consistent accounting of the probability distributions and threshold cuts in order to reduce pulse-width biases. The excellent sensitivity obtained has allowed us to probe further into the population of giant pulses. We find that a significant portion, no less than 50%, of the overall pulsed energy flux at our observing frequency is emitted in the form of giant pulses.

*Subject headings:* pulsars: general — pulsars: individual (Crab pulsar)

## 1. Introduction

While giant pulses (GPs) have been reliably detected from seven pulsars, (Knight 2006 and references therein) their properties have only been well studied from two objects, the Crab pulsar, PSR B0531 + 21 (Sallmen et al. 1999; Cordes et al. 2004; Hankins et al. 2003; Hankins & Eilek 2007), and PSR B1937 + 21 (Cognard et al. 1996; Soglasnov et al. 2004). In particular, the Crab pulsar has long been known as a giant pulse emitter. Its initial discovery (Staelin & Reifstein 1968) and a number of subsequent studies have reported remarkable properties of giant pulses from the Crab. Giant pulses are a broadband phenomenon (e.g., Sallmen et al. 1999) exhibiting the Galaxy's largest observed brightness temperature (Cordes et al. 2004), and a subset of them are, in effect, superpositions of extremely narrow nanosecond pulses (Hankins et al. 2003; Hankins & Eilek 2007). It has been shown that energy flux emission from giant pulses exhibit

a power law distribution  $N(E > E_0) \sim E_0^{-\alpha}$ , with  $\alpha$  in the range of 1.5-2.5 (Popov & Stappers 2007), in contrast to normal radio pulse emission being Gaussian distributed (Hesse & Wielebinski 1974).

In this paper we analyze high time-resolution GP observations from the Crab pulsar conducted with Goldstone's Deep Space Network (DSN) 70 m radio telescope at 1.7 GHz (L-band). With our large data sample, we carried out a number of statistical studies of GP properties. We present radio observations and a description of the recording strategies and setup in Section 2. In section 3 we present the data reduction and analysis scheme. In section 4 we provide a description of the statistical studies, followed by a discussion of the implications of the analysis. Finally, conclusions are given in section 5.

## 2. Observations and Data Set

As part of an effort to revitalize the L-band system on the DSN 70 m antenna in Goldstone, a number of pulsar observations were carried out over four epochs in early to mid 2008. The Crab pulsar was observed during two of these epochs

<sup>1</sup>Jet Propulsion Laboratory, California Institute of Technology, 4800 Oak Grove Dr., Pasadena, CA 91109.

for a total observing time of almost four hours. For these observations, the front-end electronics down-converted the L-band RF signal to IF (via an intermediate S-band up-conversion) for recording, using a pair of VLBI Science Receivers (VSRs). The VSRs filter and sample the analog IF signal, then digitally form sub-channels for recording to disk. The data used for this study consist of 32 MHz recorded bandpass in the range 1648-1680 MHz, recorded as four adjacent 8 MHz channels with 2-bit I and 2-bit Q samples for 8050 continuous seconds, followed 3 min later by two 16 MHz channels with 1-bit I/Q sampling for 1830 continuous seconds. A number of hardware problems were encountered during the experiment's first hour, including antenna pointing and recorder sampling errors. The data corresponding to these problems were removed. The configuration of the channels is summarized in Table 1.

The system temperature during Crab pulsar observations may be dominated by the emission from the Crab Nebula, one of the brightest radio sources in the sky. This is certainly true in our case, where the nebula is not resolved by the antenna beam. The nebula is an extended source with a  $\sim 5.5'$  diameter and a flux density parametrized as  $S_N \sim 955\nu^{-0.27}$  Jy (Bietenholz et al. 1997), where  $\nu$  is the observing frequency in GHz. At an observing frequency of 1.7 GHz, the nebular flux density is  $S_N \sim 830$  Jy. Since the DSN's 70 m antenna beam at L-band has a half-power width of  $\sim 8.8'$ , the nebula is not resolved so the system noise must correctly account for the nebular noise contribution. The nebular contribution  $S_N$  is combined with the contribution from the system temperature in absence of the Crab Nebula ( $S'_{sys}$ ) to obtain the total system temperature:

$$S_{sys} = S_N + S'_{sys} \quad (1)$$

On-off measurements of a standard calibrator 3C48, and bright radio pulsar PSR B0329+54 were carried out prior to observing the Crab. These observations yield a system temperature,  $S'_{sys}$ , of 35 K (10% error). Because the nominal gain  $G$  of the 70 m antenna is  $\sim 1.0$  KJy $^{-1}$ , the measured system temperature translates into a system equivalent flux density ( $S_{sys} = T_{sys}/G$ ) of 35 Jy. Adding the estimated nebular contribution of  $\sim 830$  Jy, yields a total system equiv-

alent flux density  $S_{sys} = 865$  Jy. This value agrees well with our estimates obtained from on-off measurements of the Crab, where we measured the system temperature while alternately pointing at the Crab, and  $1^\circ$  away. We estimate the error for our overall flux density calibration scale to be less than  $\sim 20\%$ . Our detection sensitivity for single pulses is determined using the radiometer equation  $\Delta S = \eta S_{sys} / \sqrt{\Delta\nu \Delta t}$ , where  $\eta$  is the digitization loss factor,  $\Delta\nu = 32$  MHz is the recorded bandwidth and  $\Delta t = 0.1 \mu s$  is the minimum sample time. With two-bit digitization we have  $\eta = 1.3$  and we obtain a  $1\sigma$  detection threshold of  $\Delta S_{min} \sim 560$  Jy. For a  $7\sigma$  detection threshold the minimum single-bin detectable pulse amplitude is expected to be 3.9 kJy. For comparison, Table 2 lists the parameters of previous Crab GP studies with the current work.

### 3. Data Reduction

Our 4 hours of Crab pulsar data, consisting of 540 Gigabytes, were recorded to disk and shipped to JPL for post-processing. The average and RMS RF voltage was computed for each second of data as a quick assessment of data quality.

#### 3.1. Coherent Dedispersion and Normalization

The data were coherently dedispersed using the nominal dispersion measure (DM) value<sup>1</sup> of 56.7671 pc cm $^{-3}$ , following the dispersion removal technique developed by Hankins & Rickett (1975). Each IF channel was dedispersed separately by performing an FFT on a full second of complex (I and Q) samples, plus the fractional second of data required to fill the FFT arrays with a power of two number of samples. For the 2-bit, 8 MHz data, the approximately 1 Hz frequency bins were counter-rotated in phase to remove the frequency-dependent dispersive delay, then inverse-transformed back to the time domain. The 1-bit, 16 MHz data were processed similarly except the final inverse FFT was performed on each half of the channel bandpass separately, effectively splitting each 16 MHz channel into two 8 MHz channels. In this way, all data could be

<sup>1</sup>The DM value was obtained from Jodrell Bank Crab pulsar monthly ephemeris:  
<http://www.jb.man.ac.uk/~pulsar/crab.html>.

TABLE 1  
VSR CHANNEL CONFIGURATION

Epoch Number	NRec <sup>a</sup>	Chan 1	Chan 2	Chan 3	Chan 4	BW (MHz) <sup>b</sup>	Nbits <sup>c</sup>	Obs Time (min)
1	2	1652	1660	1668	1676	8	2	135
2	1	1656	1672	-	-	16	1	30
3	2	1652	1660	1668	1676	8	2	75

<sup>a</sup>Number of recorders

<sup>b</sup>Channel Bandwidth

<sup>c</sup>Number of recorded bits per sample

TABLE 2  
CRAB PULSAR GIANT PULSE OBSERVATIONS

$\nu$ (GHz) <sup>a</sup>	Epoch (MJD)	T (hr)	BW (MHz)	$\Delta T$ ( $\mu$ s)	SEFD <sup>b</sup>	Ndet <sup>c</sup>	Telescope	Reference
0.1-0.2	53635	-	6	1024-256	1100	31	MWA-LFD	(Bhat et al. 2007)
0.430	52304	1.0	12.5	128	1262	11880	Arecibo	(Cordes et al. 2004)
0.6/1.4	50224	-	50	1	-	29	VLA	(Sallmen et al. 1999)
0.812	48433	100	20	200-300	13.5	$3 \times 10^4$	GB 43m	(Lundgren et al. 1995)
1.18	52277	0.47	100	100	309	863	Arecibo	(Cordes et al. 2004)
1.197	52944	3.5	20	4	215	17869	WSRT	(Popov & Stappers 2007)
1.475	52277	0.58	100	100	291	647	Arecibo	(Cordes et al. 2004)
1.3-1.47	53736	3	64	0.5	1100	706	ATCA	(Bhat et al. 2008)
1.7	54618	3	32	0.1	865	2500	Goldstone	This paper
2.15	52304-52306	0.15	100	32	79	135	Arecibo	(Cordes et al. 2004)
2.33	52315	0.15	100	32	78	92	Arecibo	(Cordes et al. 2004)
2.85	52306	0.26	100	32	74	103	Arecibo	(Cordes et al. 2004)
3.5	52398-52412	1.27	100	64	41	549	Arecibo	(Cordes et al. 2004)
4.15	52295-52337	1.49	100	32	20	1663	Arecibo	(Cordes et al. 2004)
4.5-10.5	53005-53736	-	2200	0.0004	-	380	Arecibo	(Hankins & Eilek 2007)
5.5	52336-52411	0.3	100	32	20	22	Arecibo	(Cordes et al. 2004)
8.8	52398-52414	1.42	100	16	22	2249	Arecibo	(Cordes et al. 2004)

<sup>a</sup>For comparison convenience this table is sorted by lowest observing frequency in ascending order

<sup>b</sup>System equivalent flux density (Jy)

<sup>c</sup>Number of detected GPs

further processed in a similar manner. Dedispersing a full second of data kept delay smearing over each  $\sim 1$  Hz frequency bin much less than a sample, ensuring the dedispersed data maintained its full time resolution.

After dedispersion, we form each sample's normalized power,  $P_i$ , averaged over all four frequency channels, where  $i$  is the sample number. This was done by independently normalizing each complex component (I and Q) from all four frequency channels so that all eight quantities had zero mean and unit standard deviation. These eight quantities were squared and averaged to form our power time series, using:

$$P_i = \frac{1}{8} \sum_{k=1}^4 (I_k^2 + Q_k^2), \quad (2)$$

where  $k$  runs over the four frequency channels. Assuming each I and Q component is normalized and Gaussian distributed, in the no-signal limit  $P_i$  will have a *reduced* chi-squared distribution with eight degrees of freedom.

### 3.2. Pulse Detection

Our pulse-detection algorithm begins with the 8 MHz  $P_i$  time series whose noise component is nominally modeled by the reduced chi-squared distribution with 8 degrees of freedom. In general, with  $\nu$  degrees of freedom, the reduced  $\chi^2$  probability density function, parameterized by  $x$ , is given by:

$$\text{pdf}(x) = \frac{\nu(\nu x)^{(\nu-2)/2} e^{-\frac{\nu x}{2}}}{2^{\nu/2} \Gamma(\nu/2)}, \quad (3)$$

where the  $\Gamma$  function for integer and half-integer arguments is defined as:

$$\Gamma(n) = (n-1)!, \quad \Gamma\left(\frac{1}{2}n\right) = \frac{(n-2)!!\sqrt{\pi}}{2^{(n-1)/2}}. \quad (4)$$

The red data points in Figure 1a show the measured  $P_i$  distribution for 30 minutes of data. The data samples were taken during the Crab pulsar off-pulse regions of the pulse phase. The black solid curve in 1a is the corresponding theoretical expectation given by Equation 3 with  $\nu = 8$ . Excellent agreement is seen in over eight decades.

In the time domain, our matched filter algorithm averages  $N$  temporally consecutive  $P_i$  power samples, and compares this with a threshold parameter designed to strongly reject noise while passing GPs with high efficiency. The filter used in this analysis begins with the  $P_i$  power series corresponding to  $N=1$ . The  $N=2$  time series is formed by averaging each consecutive pair (without overlap) of the  $N=1$  series, resulting in half the number of power samples. This doubling procedure is repeated up to the creation of the  $N=2048$  power series which corresponds to  $256 \mu\text{s}$  wide time-averaged bins. For each power series, summing over the  $N$  samples results in:

$$P_i^N = \frac{1}{N} \sum_{m=0}^{N-1} P_{i+m} \quad (5)$$

where  $i$  is in the range  $(0, N, 2N, \dots)$ . Because each  $P_i$  averages 8 Gaussian squares,  $P_i^N$  will have its noise component distributed according to Equation 3 with  $\nu = 8N$ , assuming the data samples  $P_i$  are truly independent.<sup>2</sup> Figure 1a shows the off-pulse power,  $P_i^N$ , for  $N = 1$  (red points  $\nu = 8$  in Equation 3),  $N = 2$  (green curve,  $\nu = 16$ ) and  $N = 4$  (blue curve,  $\nu = 32$ ). The black curves give the theoretical distributions from Equation 3 in each case.

In order to prevent cut-induced biases in the giant-pulse width distribution, proper threshold cuts should result in the same number of background noise events per second, on average, regardless of  $N$ . We define  $R$  to be the rate of noise fluctuations expected to pass a threshold cut  $\xi(N)$ , in units of events per second. This is equivalent to picking a constant event confidence level independent of pulse width. The noise rate  $R$ , also the false alarm rate, is equal to the probability that an averaged power computed with  $N$  samples exceeds  $\xi$ , times the number of trials in 1 second:

$$R(\xi) = S(\xi) \times \frac{f_s}{N} \quad (6)$$

where  $S(\xi)$  is 1 minus the cumulative probability distribution corresponding to Equation 3, also

<sup>2</sup>As  $N$  increases, a small sample-to-sample correlation was seen. This loss of true data independence was handled by making a small correction to the ideal  $\nu$ . For example, the  $N_s = 4$  case, ideally  $\nu = 32$  but  $\nu=31$  yields a better fit to the data.

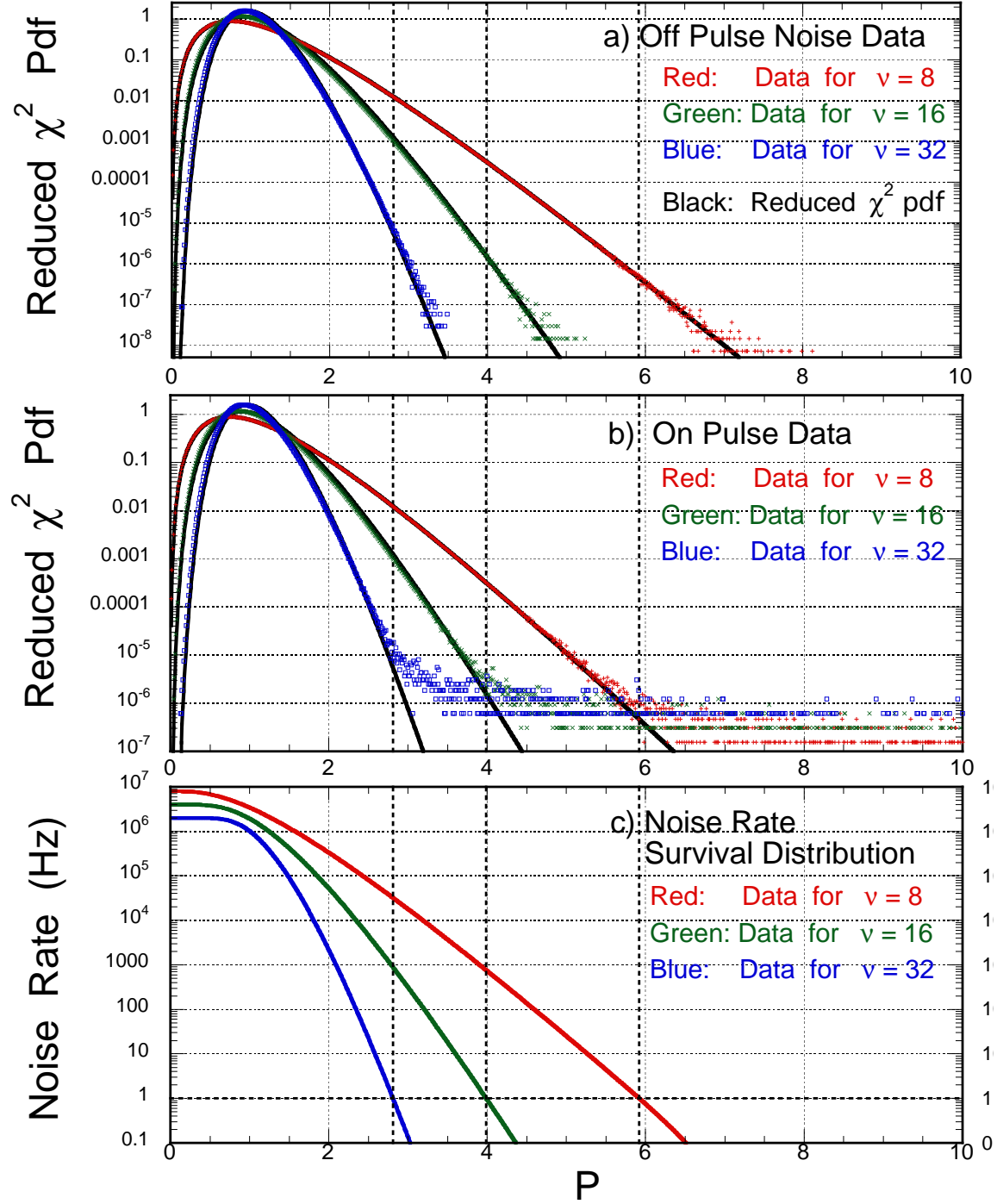


Fig. 1.— a) The background pulse  $\chi^2_\nu$  distribution for  $\nu$  of 8, 16 and 32; the red, green and blue data points respectively. b) The background pulses plus giant pulse  $\chi^2_\nu$ . The corresponding theoretical  $\chi^2_\nu$  distributions are the solid black curves. c) The noise rate survival distribution for  $\nu$  of 8, 16 and 32; the red, green and blue curves respectively. The black horizontal dashed line, at a noise rate of 1 Hz, intersects the three  $\chi^2_\nu$  distributions at the corresponding power cut points. Three black vertical dashed power cut lines have been extended through all three figures.

known as a survival function, and  $f_s$  is the number of samples per second. Figure 1c shows the noise rate as a function of  $P$  for the  $N = 1$  (red points),  $N = 2$  (green curve,  $\nu = 16$ ) and  $N = 4$  (blue curve,  $\nu = 32$ ) cases.

In the limit of large  $\xi$ , reasonable given our desire to strongly cut noise, this becomes:

$$R = \frac{f_s}{N} \frac{(4N\xi)^{4N-1} e^{-4N\xi}}{(4N-1)!}. \quad (7)$$

The threshold values are computed from this equation iteratively using

$$\xi(N) = \frac{1}{4N} [(4N-1)\log(\xi) - \log(R) + C] \quad (8)$$

where

$$C = (4N-1)\log(4N) + \log\left(\frac{f_s}{N}\right) - \log((4N-1)!) \quad (9)$$

For each averaged power  $P_i^N$  in every power series, Equations 7 and 8 are used to compute the effective noise rate  $R$  corresponding to the measured  $P_i^N$ . This effective noise rate estimates the likelihood that a given averaged power value is a noise fluctuation. The dotted horizontal line in Figure 1c is the 1 Hz rate cut,  $R\text{-cut}=1.0$  Hz, and the corresponding power cuts  $\xi(N=1)$ ,  $\xi(N=2)$  and  $\xi(N=4)$  are shown as the three vertical dotted lines in Figure 1a and Figure 1b. As described below, we reduce background noise by cutting on  $R$ , using the  $\xi(N)$ , in order to guarantee that the background rate is independent of  $N$ .

This consistent accounting of the probability distributions and equivalent threshold cuts to keep background rates independent of pulse width ensures balanced detection efficiencies even for extremely large-width giant pulses.

Figure 1b plots the  $\chi_\nu^2$  distributions for all the data, so as to include the Crab's giant pulses: the long tail of events with large  $\chi_\nu^2$  is clearly seen. With each detection, both  $N$  and the probability of such a pulse being a noise fluctuation, expressed as  $R$  in Equation 7, are stored.

This pulse-detection algorithm typically detects each pulse candidate a large number of times, so a method is needed to transform these multiple detections into individual pulse candidates, and to estimate their properties such as time, total power, and width. The algorithm used in this

analysis was to flag any sample that participates in a detection, regardless of  $N$ , then call any contiguous interval of flagged samples a pulse candidate. A number of parameters were computed for each pulse candidate. The peak power, the pulse integrated power, the time at peak power, the power-weighted mean pulse time, and the power variance about the mean time, were all computed from the 8 MHz channel-summed powers. From the multiple detections associated with each pulse candidate the lowest-probability  $R$ , corresponding to the highest significance, was chosen as the giant pulse. The associated  $N$ , power, and time were then saved.

Figures 2a and 2b show scatterplots of pulse phase and time for all giant pulses found in our data set, for both a relatively soft ( $R=0.02$  Hz) and hard cut ( $R=0.0006$  Hz), respectively<sup>3</sup>. The main pulse, with phase near 0.3, and the interpulse, near 0.7, are clearly evident. The loose R-cut (0.02 Hz) implies more white-noise contamination due to the corresponding lower  $\chi_\nu^2$  thresholds. Similarly, the tight R-cut (0.0006 Hz) reduces noise contamination on higher  $\chi_\nu^2$ , which is equivalent to a higher power signal-to-noise (SNR) threshold. The projections of these scatterplots onto the time axis, the pulse phase histograms, are presented in Figures 2c and 2d for the hard and soft cut, respectively. In the loose-cut case, over 1600 main giant pulses (GPs) are seen on a flat background of 100 noise pulses. With tight cuts, over 1200 main pulse GPs are found with no background, and a clear peak of GPs is seen at the interpulse phase region. By defining an on-pulse phase range of (0.32, 0.35) for the main pulse phase, and (0.72, 0.75) for the interpulse phase, we can study the count rate and SNR of the GPs as a function of  $R$ -cut.

If  $S_T$  is defined as the number of counts within the on-pulse region and  $S_N$  is the number of background counts estimated from the off-pulse phase region, the background-subtracted signal count is  $S = S_T - S_N$ . Assuming counting statistics, the SNR is then:

$$SNR = (S_T - S_N)/(S_T + S_N)^{1/2} \quad (10)$$

<sup>3</sup>The significance of these cut values becomes clear later in the paper.

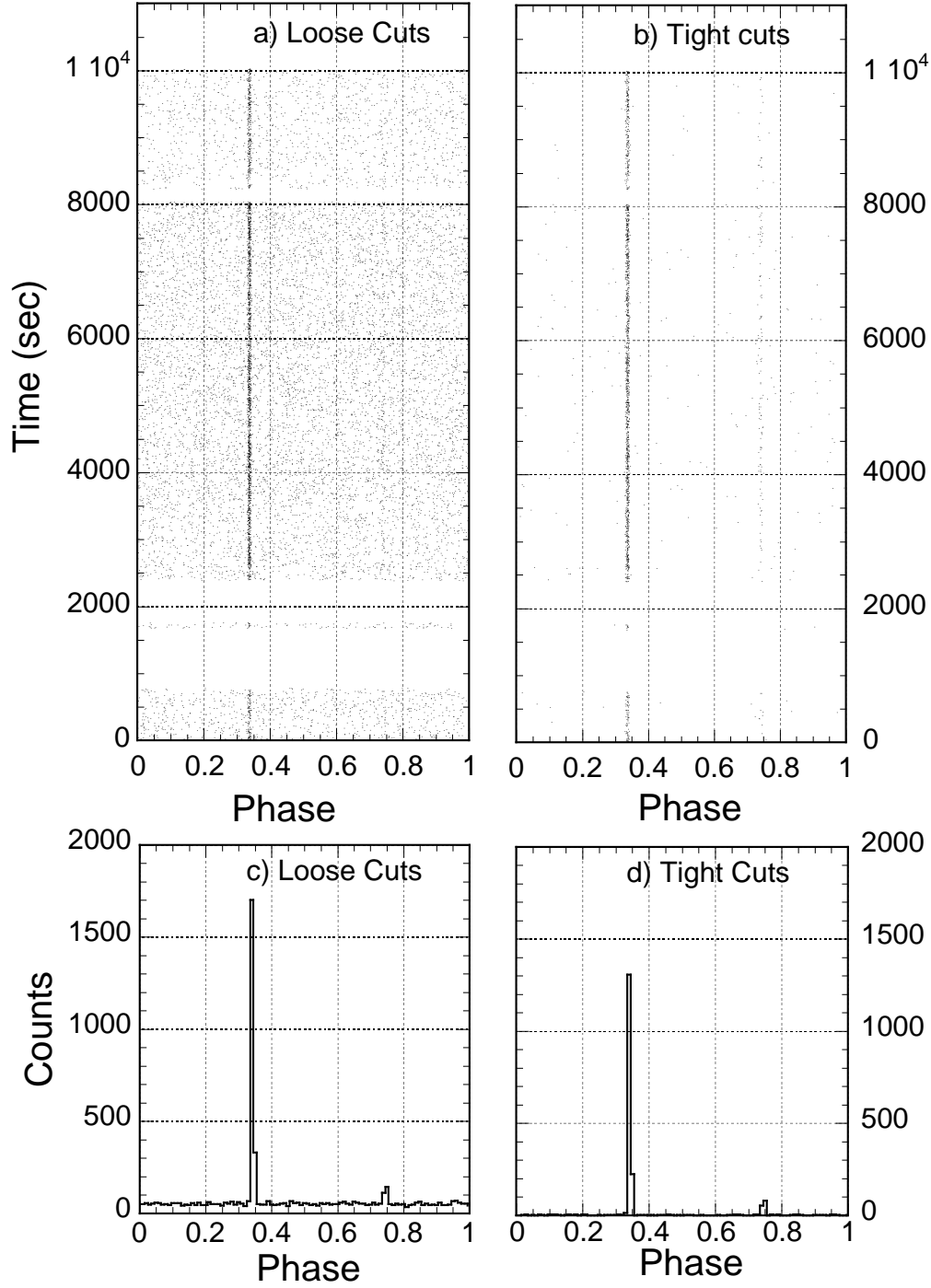


Fig. 2.— Time phase scatterplots of the detected pulses for the loose and tight data sets. The main and interpulse giant pulses are seen as straight lines at phases of 0.337 and 0.737 respectively. The bottom histograms shows the corresponding phase projection. The improvement in signal to noise is clearly seen with the tight cuts.

Figure 3 shows the total number of giant pulses as a function of  $R$ -cut, for both the main and interpulse regions. For the loosest cut processed ( $R=0.6$ ), over 2500 main phase GPs and 200 inter phase GPs are observed.

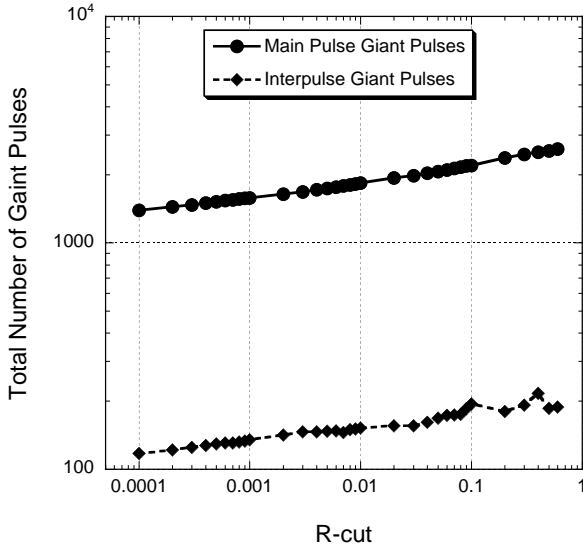


Fig. 3.— The number of background-subtracted Giant Pulses, for both the Main pulse and Interpulse, as a function of the noise cut,  $R$ -cut. As the  $R$ -cut increases (power amplitude cut decreases) the total number of giant pulses increase.

Careful examination of the pulse-candidates in Figure 2a shows density variations during the experiment's first and last hours. Our detection thresholds were adjusted to allow an approximately constant noise rate as a function of pulse width, however Figure 2a shows that the noise rate is not constant in time. At the experiment's start, there were a number of problems with the front-end sampler voltage thresholds, which reduced the data sensitivity. The single-bit data beginning at time 8230 s also shows a low pulse-candidate density. Even though dispersion mitigates the 1-bit sampling loss to some extent, as explained above, these data are somewhat less sensitive than the 2-bit data. Efforts to reconcile the different sampling effects and resulting sensitivities, for example by scaling the sample values or modifying the detection thresholds, significantly increases the complexity of the analysis. Thus, from this point forward the analysis is restricted to only those data taken from time 2400 to 8050 s,

a total of 5650 seconds of data, as these data have the highest sensitivity, and show an approximately constant sensitivity.

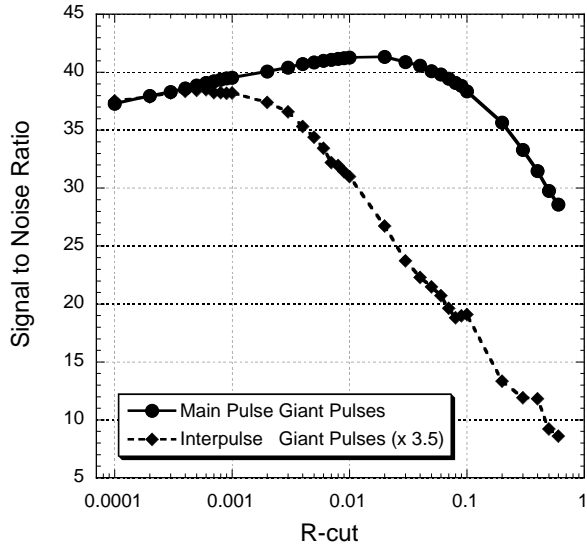


Fig. 4.— The giant pulse signal-to-noise ratio as a function of the noise cut,  $R$ -cut, for both the main pulse and interpulse GPs.

Figure 4 shows the SNR as a function of  $R$ -cut for both the main and interpulse pulses. It is seen that the maximum SNR for the main pulses are at  $R = 0.02$  and  $R=0.0006$  respectively. lowering the  $R$ -cut (increasing the total  $\chi^2_\nu$  cut) fewer GPs with higher SNR values are detected. In this paper we will refer to three cuts, a loose cut at  $R=0.02$ , a tight cut at  $R=0.0006$ , and the loosest cut at  $R=0.6$  resulting in the largest sample of Main Pulse (MP) GPs found in this analysis ( $\simeq 2500$ ). Yet even with the tight cut over 1200 MP GPs and over 100 Inter-Pulse (IP) GP are detected both without any significant background contamination.

#### 4. Various Statistics of Detected Giant Pulses

The tremendous amount of energy radiated by giant pulses is observed with a wide variety of pulse morphologies. One of the goals of giant-pulse research is to determine, as closely as possible, the originating pulse shape, its amplitude and width. A wide variety of factors influence the shape of the pulse, such as dispersion, in-



strumental smearing, interstellar scintillation and scattering due to turbulent media. These effects all tend to broaden a pulse, decreasing its true peak amplitude and increasing its width. In our data set, the amplitude is simply defined as the peak power, or rather the peak flux density, found in the optimum smoothed data set. Past attempts to characterize pulse widths for a large sample of GPs have been limited either to coarse sampling size or large dispersive smearing and small sample sizes (Lundgren et al. 1995; Popov & Stappers 2007; Bhat et al. 2008). Our L-band observations, employing coherent dedispersion on large bandwidth baseband channels minimize the dispersive smearing, obtaining a 125  $\mu$ s time resolution, contain over 1200 GPs, which should allow more robust width measurements.

#### 4.1. Pulse Amplitudes and Widths

Visual examination of many pulses, some of which are shown in Figures 5a-f, reveals that variations in pulse morphology represent the dominant systematic error in pulse amplitude and width determinations. The six GP events shown are plotted using their optimum smoothing, with widths ranging from the narrowest (smoothing widths of  $N=4$ ) to the widest ( $N=512$ ), and with amplitudes ranging from 1 kJy to above 100 kJy. Although a large subset of GPs can be well fit to a Gaussian shape, an equally large sample of GPs show non-Gaussian shapes, as presented in Figures 5c-f. Given a significant fraction of GPs having non-Gaussian shapes, fitting GPs with a Gaussian model yields poor chi-squared fits, and thus poor amplitude and width estimates.

An alternative width definition is simply the optimum smoothing width  $W_s = N\Delta t$  ( $\Delta t$  is the intrinsic sample resolution) obtained from the giant pulse detection algorithm. The amplitude and timing can then be defined using the bin with the greatest power amplitude. With these alternative definitions of power amplitude and width, pulse morphology can be seen in Figure 6a, where the scatter plot shows GP peak flux density versus width, for all the GPs passing the tight-cut. A strong correlation between the observed peak flux density and smoothing width is observed, with higher peak flux density seen at lower smoothing widths. The diagonal dotted lines in Figure 6a show iso-energy flux contours of 1 kJy- $\mu$ s, 10 kJy-

$\mu$ s and 100 kJy- $\mu$ s. A wide variation of shapes can be seen for the same observed energy flux. For example, a large pulse with  $E = 10$  kJy- $\mu$ s can be very sharp, less than a  $\mu$ s in width with over 10 kJy peak flux density, or very broad, with widths over 10  $\mu$ s but flux density less than 1 kJy. Although great care was taken to ensure that no pulse width selection bias occurred, a comparison of the GP data with the iso-energy flux contours suggests that giant pulses with total energy fluxes of  $\sim 1$  kJy- $\mu$ s cannot be extracted above smoothing widths of 2  $\mu$ s.

Figures 6b and 6c show the corresponding amplitude and width projections. The peak flux density distribution in Figure 6b indicates the median pulse flux density is  $\sim 1$  kJy with a minimum observed peak flux density of  $\sim 0.1$  kJy and a maximum of  $\sim 100$  kJy. Above a peak flux density of 2 kJy, the histogram shows a power-law dependence out to 100 kJy. A power-law fit yields an exponent of  $\alpha = -2.2 \pm 0.1$ , very close to that found by (Bhat et al. 2008), where at slightly lower frequencies of 1300 MHz and 1460 MHz, values of -2.3 and -2.2 were measured respectively.

The distribution of the smoothing width,  $W_s$ , is shown in Figure 6c. The median  $W_s$  is 2  $\mu$ s and the mean  $W_s$  is  $\sim 6$   $\mu$ s with a minimum of 0.2  $\mu$ s with a long tail extending out to 100  $\mu$ s. This width range compared to previous Crab GP datasets (Bhat et al. 2008) is extended to pulses with 10 times wider and two times narrower widths.

Although the smoothing width,  $W_s$  is a convenient definition of pulse width, it does not always appear to be optimum. Sometimes, as shown in Figure 5b, a wide giant pulse with  $N=512$  has almost all its energy within the one smoothed bin. Yet as Figures 5c-f illustrate, a large fraction the time significant energy is spread over many bins at the optimum smoothing width. Following others (Bhat et al. 2008) we define an “effective pulse width,”  $W_{std}$ , which is the standard deviation (std) for all “acceptable” bins in a giant pulse, where acceptable bins are defined with a simple algorithm. Raw data with the highest time resolution is used, and data within  $\sim 3N$  of the maximum power amplitude sample is selected. Only bins with power amplitudes greater than 2 sigma above the background power are included in the first estimation of the  $W_{std}$ , and the background level. The final calculation sums over all bins

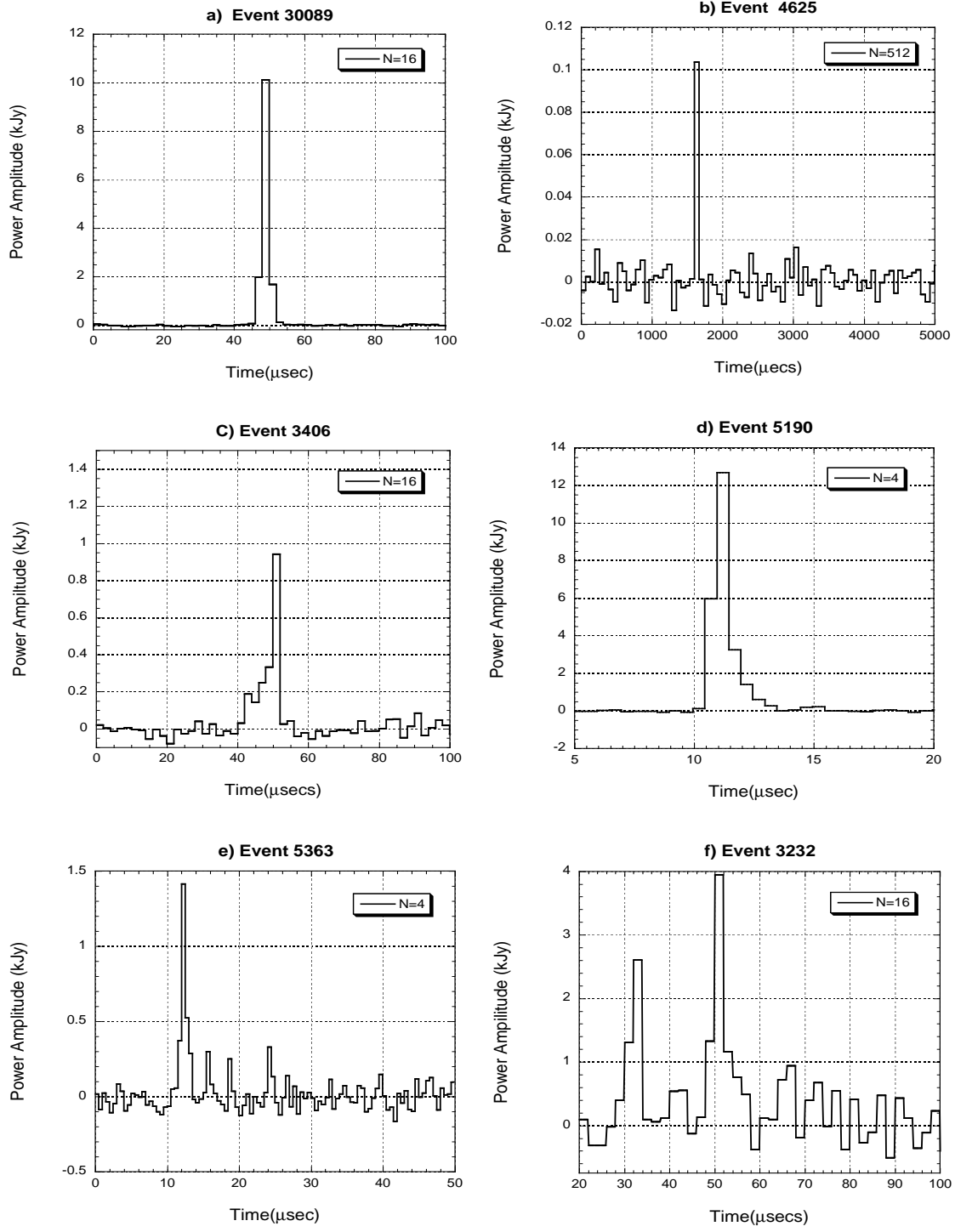


Fig. 5.— Giant pulse time series plots. Each is shown with it's optimum smoothing width "N". The widest pulse shown is pulse b with N=512 and the two narrowest shown are pulses d and e with N=4

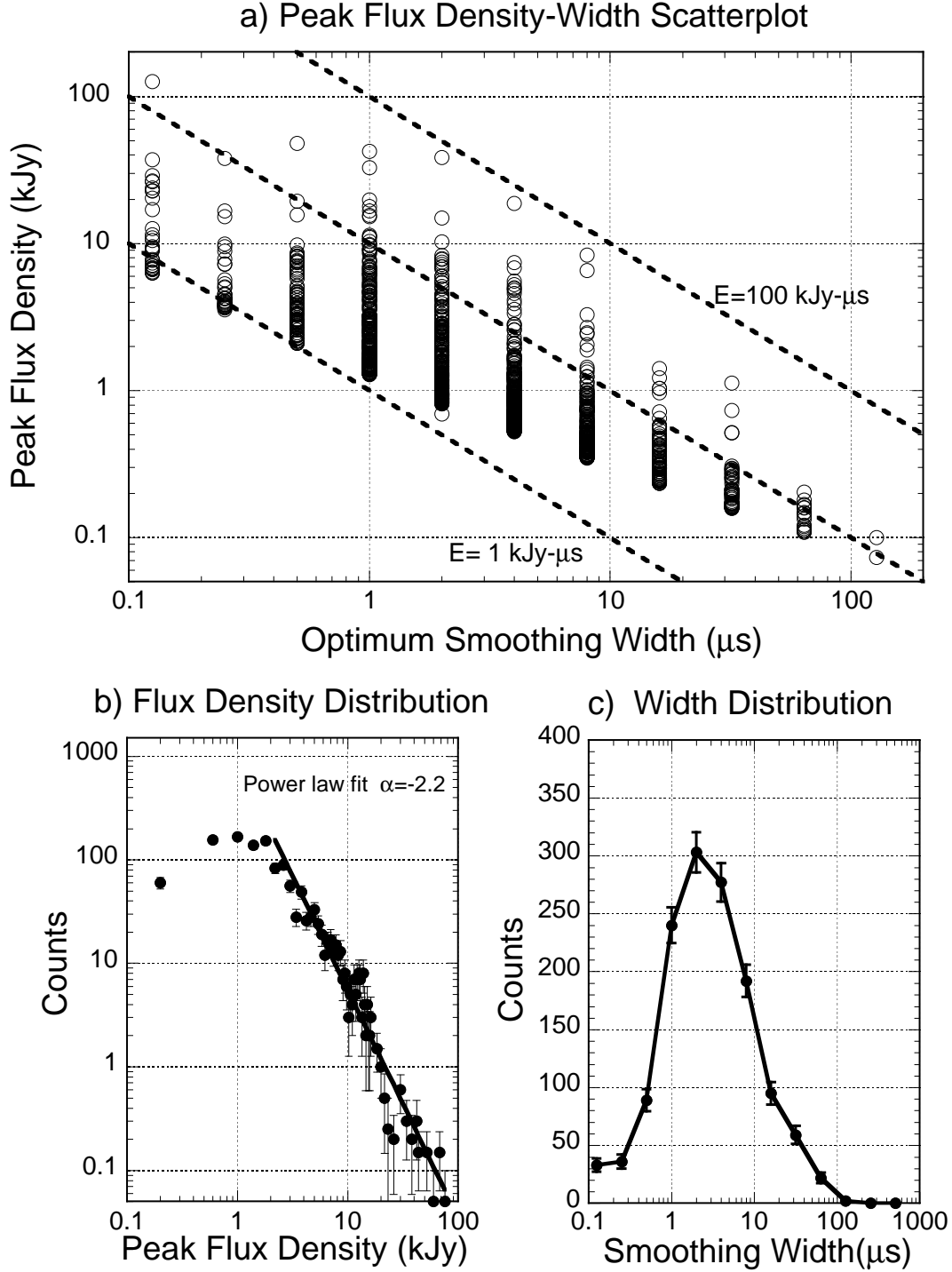


Fig. 6.— The scatterplot of peak flux density and optimum smoothing width ( $W_s$ ) along with the corresponding peak flux density (b) and width projection histograms (c) for the tight cut. The diagonal dotted lines in the scatterplot (a) are energy isotherms at  $E=1 \text{ kJy-}\mu\text{s}$ ,  $10 \text{ kJy-}\mu\text{s}$  and  $100 \text{ kJy-}\mu\text{s}$

within  $\sim 3W_{std}$  of the peak, again with bins having power amplitudes greater than 1 sigma above the background. This algorithm allows us to estimate the pulse standard deviation and higher order moments such as skewness and kurtosis. This procedure gives an estimate of the pulse width ( $W_{std}$ ) that, as expected, gives excellent agreement with the fitted Gaussian sigma and gives a reasonable estimation of the pulse width in the non-Gaussian cases. A comparison with pulse widths extracted by Bhat et. al., at 1470 MHz, can be seen in Figure 7. Due to the higher time resolution in this study, pulses with widths a factor of 2 narrower are detected. Perhaps the more significant difference with the earlier data of Bhat et. al. is the increase in the sensitivity at very large pulse widths. Bhat et. al. observed no pulses with widths greater than 10  $\mu s$ , whereas the present data set has a significant number of pulses extending out to over 100  $\mu s$  with a median  $W_{std}$  of 2.35  $\mu s$  and a mean of 10.45  $\mu s$ . We have parameterized this distribution with a good power law fit,  $N(W_{std}) \propto W_{std}^{-1.3}$ , that extends from  $\sim 1 \mu s$  to almost 100  $\mu s$ .

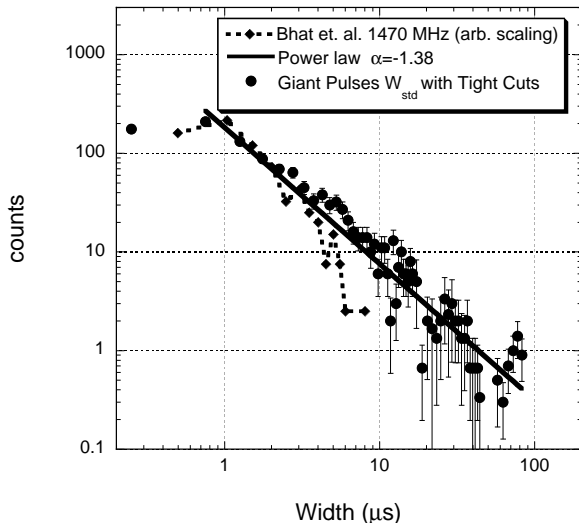


Fig. 7.— The giant pulse width histogram for the tight data set. The fitted power law is indicated by the solid line. The dotted histogram is data of (Bhat et al. 2007)

#### 4.2. Pulse Energies

The measurement of giant pulse parameters such as power amplitude, width, and energy flux

are critical in constraining models of GP emission. The total pulse energy flux has the advantage, as compared to pulse width, of being a robust pulse estimation parameter, as it is relatively insensitive to pulse shape. Also, since the total pulse energy flux is a simple power sum over the pulse duration, the random background noise will tend to average down to zero. The GP energy flux distribution, for the tight cut data set, is shown as black circles in Figure 8. Energy fluxes up to  $\sim 100 \text{ kJy-}\mu s$  are found, consistent with earlier studies (Bhat et al. 2008). The average observed GP energy flux for all the main giant pulses was  $\sim 7 \text{ kJy-}\mu s$  with a median energy flux of  $\sim 5 \text{ kJy-}\mu s$ . Above 5  $\text{kJy-}\mu s$  the data are well fit by a power law, the solid line in Figure 8 shows fit to the data with  $\alpha = -2.57$ . A very sharp energy flux threshold is observed at  $\sim 3 \text{ kJy-}\mu s$ . The black diamonds in Figure 8 show the main GP energy flux distribution for the loosest cut examined. An additional  $\sim 1400$  main GPs are found but all at lower energy flux as would be expected. The additional main GPs seem to follow the same power law as the data with tight cuts but the energy threshold is reduced to  $\sim 1.5 \text{ kJy-}\mu s$ . No evidence is seen for a roll over or softening of the intrinsic power law. The turnover in Figure 8 is most likely due to the applied threshold cut.

Following a previous analysis (Knight 2006), the cumulative energy flux distribution, defined as the probability per second of a pulse having an energy flux  $E$  greater than a value  $E_0$ , is used to compare the occurrence frequency of giant pulses between different experiments:

$$P(E > E_0) = kE^\alpha \quad (11)$$

Figure 9 shows the observed cumulative energy flux distribution for the tight data set, solid black circles, along with the data from Bhat et. al., open squares. The solid line is a power-law fit to the data in the energy range 5 to 100  $\text{kJy-}\mu s$ . Above the energy flux threshold, the data are well fit by a power law and no evidence is found for high-energy flux cut-offs. The best-fit power law exponent is found to be  $\alpha = -1.9 \pm 0.05$ . The agreement with Bhat et. al. is very good in the energy flux region of 10-20  $\text{kJy-}\mu s$  but significant differences in slope and absolute magnitude are seen at higher and lower pulse energy fluxes. This disagreement can be understood by a combination of differences in

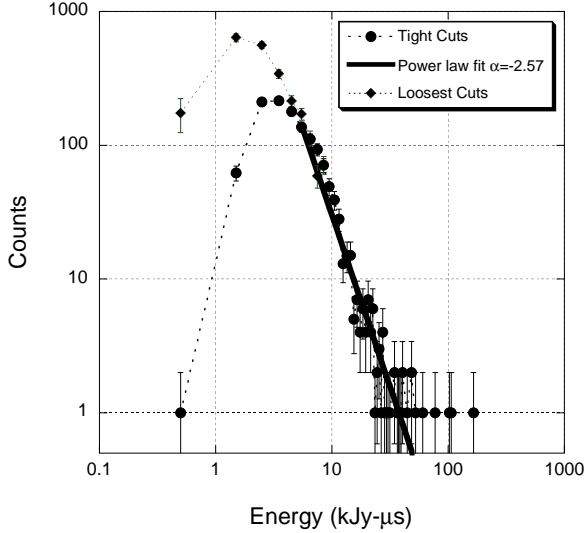


Fig. 8.— The giant pulse energy flux distribution with a power law fit of  $\alpha = -2.57$  for energy fluxes between 5 and 50 kJy- $\mu$ s.

antenna sensitivity and pulse algorithm efficiency. As discussed earlier, for any fixed pulse energy a wide range of pulse amplitudes and widths are observed. A loss of pulse detection efficiency at low and high widths may alter the true nature of the cumulative energy flux distribution.

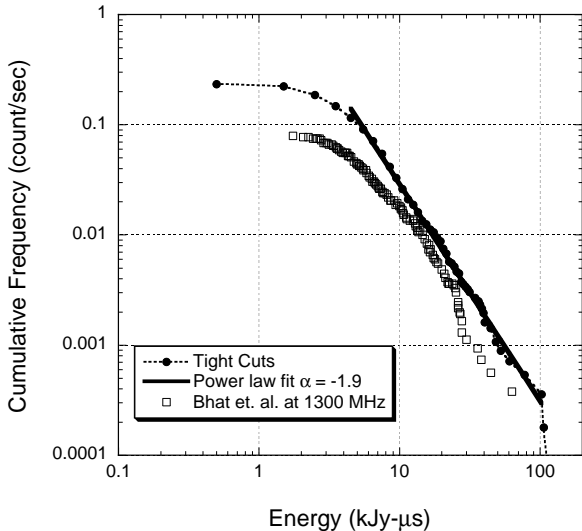


Fig. 9.— The cumulative energy flux distribution for giant pulses. A power law fit for energies above 5 kJy- $\mu$ s yields  $\alpha = -1.9$ .

Although earlier work by Bhat et al. (Bhat et al. 2008) only covered widths from 1 to 10  $\mu$ s, others (Popov & Stappers 2007) found a dependence on pulse width, such that at narrow widths ( $\sim 4 \mu$ s),  $\alpha = -1.7$  whereas for wider pulses (65  $\mu$ s),  $\alpha$  was found to be  $-3.2$ . To examine this dependence our tight data set was divided up into two subsets: a narrow ( $W_s$  less than 5  $\mu$ s) and a wide data set ( $W_s$  greater than 5  $\mu$ s). In both cases, the slope of the cumulative energy flux distribution was estimated. The narrow data set yields a slope values of  $-1.7$  to  $-2.0$ , dependent on the energy flux range fit, which is very consistent with Bhat et al. While the wide data set yields a steep slope of  $\alpha = -2.4$  to  $-3$ , consistent with the work of Popov and Stappers.

It is interesting to compare the total energy flux emitted by the Crab pulsar as giant pulses with the overall pulse emission at this frequency. Using the background-free data set (tight cuts), we summed the energy flux of each candidate GP, obtaining an average pulse energy flux of 0.134 kJy- $\mu$ s per rotation over the span of the observation, which amounted to  $\sim 168,000$  rotations. On the other hand, the mean pulse energy flux from the pulse profile containing all rotations is 0.26 kJy- $\mu$ s. This value is in excellent agreement with the quoted value in the ATNF catalog<sup>4</sup> after extrapolating the mean flux density from 1400 MHz to 1665 MHz using their spectral index of  $-3.1$ . This suggests that a significant fraction, at least  $\sim 50\%$ , of the pulsar emission energy may be emitted as GPs. Another estimate for pulse energy flux obtained at a frequency of 1664 MHz, nearly identical to our observing frequency, suggests a mean energy flux of 0.125 kJy- $\mu$ s for the main pulse and 0.025 kJy- $\mu$ s for the interpulse at this frequency (Manchester 1971). The total energy flux amounting to 0.15 kJy- $\mu$ s is very close to the entire GP energy flux emission, further suggesting that a significantly large portion of the energy flux may be emitted as GPs.

As a further check we compared the pulse profile including all rotations with a second profile, where rotations containing an identified GP is removed from the profile. Figure 10 shows the two pulse profiles. The second profile (dashed curve)

<sup>4</sup>ATNF pulsar catalog web address:  
<http://www.atnf.csiro.au/research/pulsar/psrcat>

is obtained using a loose cut to identify GP candidates. The figure shows that GPs make up 54% of the overall pulse energy flux at our observing frequency. Also, evident from the figure is how identical the two profiles are in terms of the pulse width. At the moment we do not have sufficient statistics to resolve and quantify the width of each profile and instead rely on a rough visual estimate. This is further indication that a similar significant reduction in energy flux is obtained assuming that the GP and main pulse widths are similar.

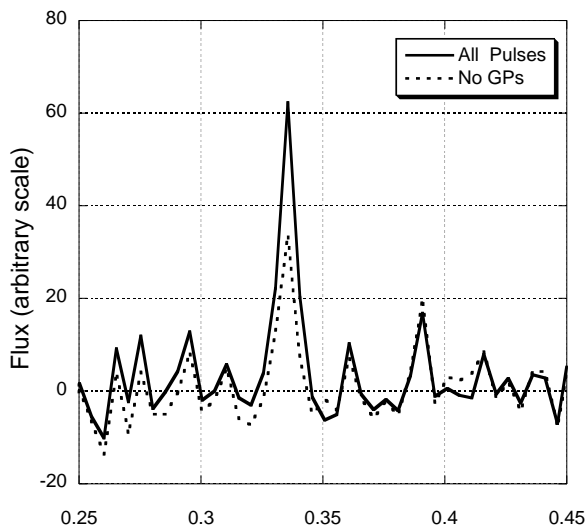


Fig. 10.— Crab pulse profiles obtained (solid curve) using the entire sample discussed in this analysis. The dashed curve shows the profile without rotation cycles that include a GP candidate.

A large fraction of the emission energy flux at this frequency is already accounted for with GPs identified at our current sensitivity. If the power law continues to lower energies, further improvement in sensitivity will allow us to reach the intrinsic turnaround in the distribution necessary to keep the total GP emission energy below the total pulsed energy. In this case, there would be only one fundamental process responsible for the total pulsed emission in the Crab pulsar.

### 4.3. Pulse Asymmetry and Shape

Skewness can be used as a measure of GP asymmetry, and is defined here to be:

$$s = \Sigma W_i(t_i - t_p)^3 / (\Sigma W_i)\sigma^3, \quad (12)$$

where the weighted sum is over a narrow region of the pulse with respect to its peak position  $t_p$ . The weight,  $W_i$ , is the power amplitude level in the corresponding time bin,  $\sigma$  is the standard deviation ( $W_{std}$ ) and the pulse algorithm used is the same as that used for obtaining the pulse standard deviation. For a Gaussian shaped pulse, skewness will have a value near zero. Pulses with long tails following the peak will have a positive skewness and those with tails before the peak will have negative values.

Figure 11 shows the skewness distribution for both the giant pulses and background pulses, solid and dashed histogram respectively. Both distributions show average skewness that is very close to zero with very similar spread in the distribution. No statistically strong skewness dependence was found as a function of width, amplitude or energy and no differences were found between the inter-pulse and main giant pulses.

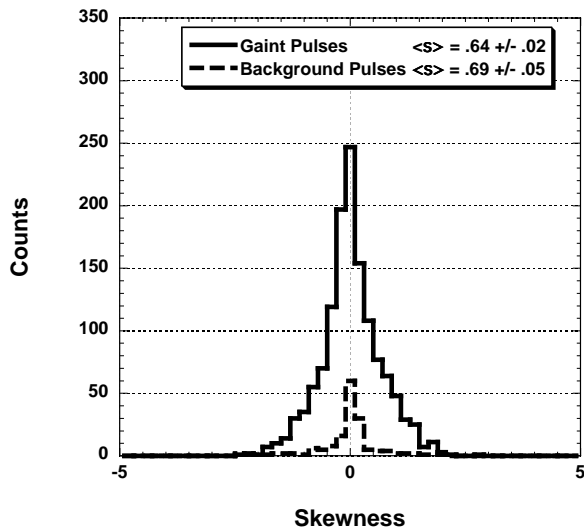


Fig. 11.— Skewness histograms for both the giant-pulses and background pulses for the tight data set.

The next higher statistical moment, kurtosis, can also yield useful information on pulse shape, and is defined as:

$$k = \Sigma W_i(t_i - t_p)^4 / (\Sigma W_i)\sigma^4 - 3. \quad (13)$$

Kurtosis is zero for a Gaussian-shaped pulse, negative for pulses that are flatter than Gaussian, and positive for pulses more steeply peaked than

Gaussian. To account for algorithmic dependences and background noise, we have calculated skewness and kurtosis for both giant pulses and out-of-phase background pulse-candidates.

Our kurtosis distribution is shown in Figure 12, for both GPs and background events. The background pulses are peaked near zero, consistent with the expectation for gaussian shaped pulses. A positive kurtosis tail extending to about a value of 5 is observed. This most likely reflects the bias of the decimation portion of the matched filter detection algorithm, where smoothing tends to increase kurtosis. The Crab’s giant pulses are seen to be peaked at a kurtosis value of 0.6 with a very long tail extending to a value of 50, implying they are more sharply peaked than pulses from the white-noise background. The reason for this can be seen by examining the dependence of mean kurtosis on the total GP energy flux shown in Figure 13. This plot shows GP averaged kurtosis increases linearly with the total energy flux. Although the background pulse candidates do not extend to high energies, it is clear their behavior is quite different from the GPs upward trend.

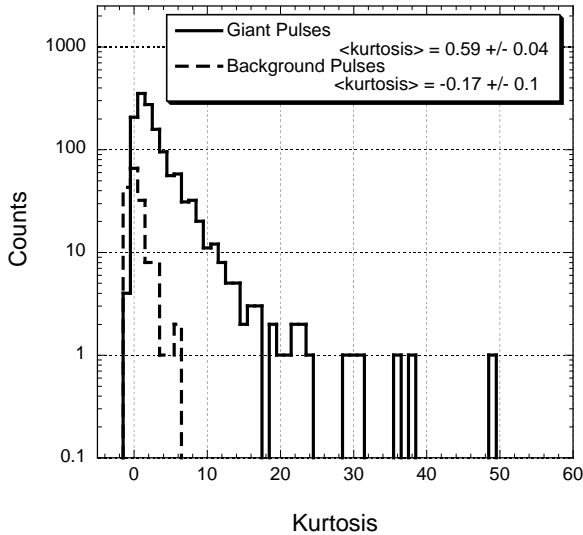


Fig. 12.— Histograms of pulse kurtosis for both giant pulses and background pulses for the tight data set.

#### 4.4. Pulse Time of Arrival

The Crab pulsar has a well defined period of  $\sim 33$  ms and the phase of the main and interpulse

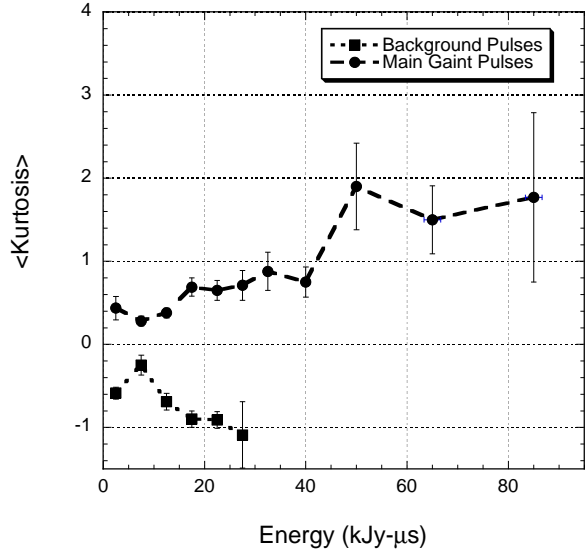


Fig. 13.— The dependence of kurtosis mean with the total pulse energy flux for the giant pulses in the tight data set.

giant pulses are well regulated within the pulsar period. The phase of both the interpulse and main pulses are seen in the projections of the scatterplot in Figure 2. The pulse phase residual, or Time of Arrival (TOA) residual, is the TOA of the GP peak with respect the start of the pulsar model cycle. For the Crab, at L-band frequency, both the main and interpulse GPs are found to have TOA residuals that fall within 1% of a cycle ( $\sim 330 \mu\text{s}$ ). Figure 14 shows the histogram for the main and interpulse GPs, where the mean TOA has been set to zero for both. To remove possible confusion in the interpulse data set due to background pulse-candidates, the tight-cut data set has been used. The main pulses are found to have rms of  $0.0028 \pm 0.0001$  cycles or  $1^\circ$  of phase corresponding to  $\sim 90 \mu\text{s}$ , while the interpulse GPs were found to be wider with an rms of  $0.0042 \pm 0.0003$  or  $1.5^\circ$  of phase corresponding to  $\sim 140 \mu\text{s}$ .

Since it is expected that the intrinsic pulse phase jitter and smearing will be independent of absolute phase location, the 50% increase in TOA width is significant and may give an important constraint in astrophysical pulsar models. Two earlier studies, both with smaller giant pulse samples, (Bhat et al. 2008; Cordes et al. 2004) found evidence for stronger pulses to have

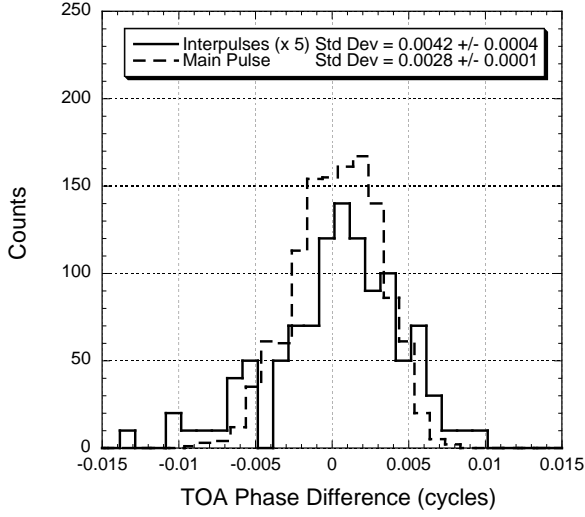


Fig. 14.— Histograms of the time of arrival for the Main and Inter-pulse Giant pulses for the tight data set.

narrower phase windows. Where strength was defined as the peak pulse amplitude. Due to the strong correlation of peak flux density and width, as shown in Figure 7a, it is reasonable to believe that the narrow widths of the larger peak pulses may indeed result in better phase resolution. To examine this possibility the tight data set was divided into two subsets, a large and small peak flux density data set, those with peak amplitude larger than 5 kJy and those smaller than 1 kJy. The widths of the TOA residuals for the two n GP samples were then estimated to be  $\sigma = 0.0027 \pm 0.0002$  and  $\sigma = 0.0027 \pm 0.0001$  for the large and small peak samples respectively. No significant difference is found, as the sample TOA residuals are seen to be statistically consistent to each other.

A plot of the main pulse energy flux versus phase is shown in Figures 15's scatterplot. No correlation between phase and energy flux is evident. To examine this more quantitatively, the data were divided into three total-energy flux classes: high energy flux ( $E \geq 200$  kJy- $\mu$ s), medium energy flux ( $100$  kJy- $\mu$ s  $\leq E \leq 200$  kJy- $\mu$ s), and low energy flux ( $E \leq 100$  kJy- $\mu$ s). The table below summarizes the TOA residual statistics of each data set. No tendency is seen for larger energetic pulses to originate in narrower phase windows.

The joint statistics of GP total energy flux with the interarrival time (IAT) of the next GP is shown

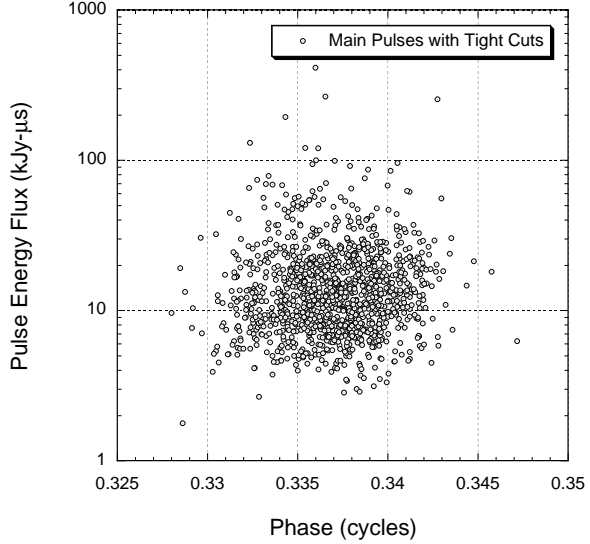


Fig. 15.— A scatterplot of the phase and total pulse energy flux.

in Figure 16. The IAT is simply the measured time between between one GP and the next. The interarrival time for both the Main pulse (MP) and Interpulse (IP) giant pulses are plotted, where the IAT is converted to the number of crab pulsar rotations ( $\sim 33$  ms). The discrete nature of the IAT for pulses below 10 rotations is simply a reflection of the phase cut (0.30-0.35) for the MPs and (0.72-0.75) for the IPs. For the sensitivity achieved with our observations, with tight cuts, the average number of Crab rotations between giant pulses was found to be 127 with the largest gap between giant pulses at  $\sim 1000$  rotations. With the loosest cut used, the averaged number of Crab rotations between GPs are 67. No observable dependence between the total GP energy flux and the arrival time of the next pulse was seen.

The smallest IAT of  $\sim 0.4$  cycle was observed twice, these cases being a main pulse immediately preceded by an interpulse (I-M). No cases of interpulse immediately following the main pulse were found in the tight data set (M-I), corresponding to an IAT of  $\sim 0.6$  cycle. To examine the independence between main and interpulses, we examined the consistency of the data with the assumed Poisson nature of the giant pulse process. A Poisson process describes events which occur continuously and independently, and for this study would imply the interarrival times are exponentially distributed



TABLE 3  
GIANT PULSE TOA RESIDUAL STATISTICS.

E ( kJy- $\mu$ s)	Sum	Mean	St.Dev.
$E \leq 100$	564	$0.3368 \pm 0.0001$	0.0028
$100 \leq E \leq 200$	571	$0.3373 \pm 0.0001$	0.0028
$E \geq 200$	106	$0.3365 \pm 0.0003$	0.0029

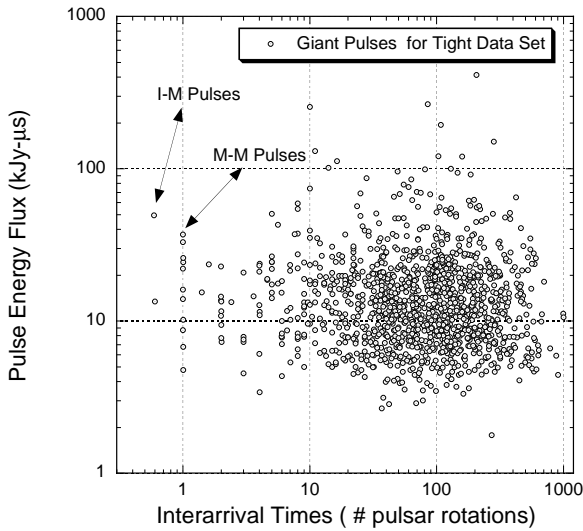


Fig. 16.— A scatterplot of the Giant-Pulse energy and Interarrival times for the Giant-Pulses in the tight data set.

with parameter  $\lambda$  (mean =  $1/\lambda$ ).

$$P(\tau) = \lambda e^{-\lambda\tau} \quad (14)$$

Figure 17 shows the distribution of MPs interarrival times along with the best fit to a Poisson model. The data appears to be consistent with a Poisson process, the best weighted fit yielding  $\lambda=0.223 \pm 0.007$  Hz with a  $\chi^2=19$  for  $\nu=23$ . This  $\lambda$  value agrees well the inverse of the mean interarrival times,  $0.234 \pm 0.007$ . Within statistics, it appears that the arrival times of Crab's giant pulses are Poisson distributed, implying they are memoryless, and any given time interval is independent of what occurs before or after.

In addition, both the interpulses and the com-

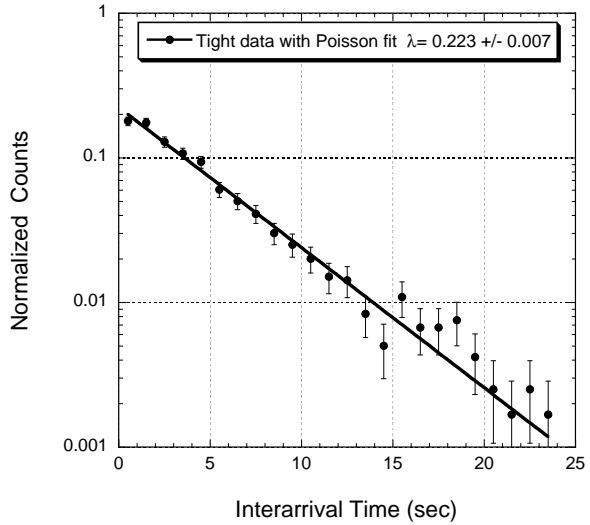


Fig. 17.— The interarrival time of main pulses (MPs) for the tight data set. The solid curve is an exponential fit to the data.

bined GP data sets show interarrival time distributions that are also consistent with a Poisson process. We conclude that interpulse GPs do not appear to be correlated with main pulses to our level of examination.

## 5. Summary and Conclusions

We have examined the energy flux distribution, timing, and statistical properties of giant radio pulses from the Crab pulsar at 1700 MHz using DSN's 70 m antenna at Goldstone, achieving a time resolution of 125 ns. Our pulse detection was based strictly on the underlying Chi-square statistics of the data, where we attempted to keep the noise rate and event confidence levels constant and independent of pulse width. Our consistent accounting of the probability distributions and non-

Gaussian effects, in order to keep background rates independent of pulse width, is an improvement over previous analyses.

The statistical analysis of giant pulse population was carried out using three significance cuts: a loose cut ( $R\text{-cut} = 0.0200$ ), where we obtained 1879 pulses, and a tight cut ( $R\text{-cut} = 0.0006$ ) yielding 1314 pulses and the loosest cut studied ( $R\text{-cut} = 0.6000$ ) which yielded over 2500 main GPs. With a large number of giant pulses we were able to study various statistical properties of GPs. We have confirmed the power-law nature of the peak pulse flux density distribution and have obtained a power-law slope of  $-2.2$ , consistent with (Bhat et al. 2008) results. We observed giant pulses with widths up to  $100\ \mu\text{s}$ , 10 times larger than the maximum found by Bhat et. al. Further, the distribution of pulse cumulative energy fluxes also follows a power-law distribution with a slope of  $-2.57$ , consistent with Bhat et al. (Bhat et al. 2008). We also looked for correlations between the time of arrival of individual giant pulses and concluded the time of arrival of each event is consistent with Poisson statistics. Our pulse detection sensitivity, high-time resolution, and consistent statistical treatment of the data has allowed us to examine a weaker population of giant pulses, narrowing the gap with "normal" pulses from the Crab pulsar.

Our comparison of pulsed energy flux emission from GPs with the normal pulsed emission has forced us to claim that a significant portion, perhaps as large as  $\sim 90\%$  but at least  $50\%$ , of the emission at this frequency is in the form of GPs. With further improvement in sensitivity and observing time, it should be possible to either confirm the turnaround seen in the energy distribution or push it only slightly lower before reaching the intrinsic turnaround in the distribution. Such a study could be carried out by a phased array instrument such as the VLA, where the narrower beam will make it possible to lower the nebular contribution to the overall system temperature, providing better sensitivity to further probe the weaker population of GPs as well as the remaining normal pulses in the system.

## Acknowledgements

We thank the staff of DSS-14 who helped in acquiring the data for this work. This work was carried out at the the Jet Propulsion Laboratory, California Institute of Technology, under a Research and Technology Development Grant. Copyright 2010. All Rights Reserved. US Government Support Acknowledged.

## REFERENCES

- Bhat, N. D. R., Tingay, S. J., & Knight, H. S. 2008, *ApJ*, 676, 1200
- Bhat, N. D. R., et al. 2007, *ApJ*, 665, 618
- Bietenholz, M. F., Kassim, N., Frail, D. A., Perley, R. A., Erickson, W. C., & Hajian, A. R. 1997, *ApJ*, 490, 291
- Cognard, I., Shrauner, J. A., Taylor, J. H., & Thorsett, S. E. 1996, *ApJ*, 457, L81+
- Cordes, J. M., Bhat, N. D. R., Hankins, T. H., McLaughlin, M. A., & Kern, J. 2004, *ApJ*, 612, 375
- Hankins, T. H., & Eilek, J. A. 2007, *ApJ*, 670, 693
- Hankins, T. H., Kern, J. S., Weatherall, J. C., & Eilek, J. A. 2003, *Nature*, 422, 141
- Hankins, T. H., & Rickett, B. J. 1975, *Methods in Computational Physics*, 14, 55
- Hesse, K. H., & Wielebinski, R. 1974, *A&A*, 31, 409
- Knight, H. S. 2006, *Chinese Journal of Astronomy and Astrophysics Supplement*, 6, 020000
- Lundgren, S. C., Cordes, J. M., Ulmer, M., Matz, S. M., Lomatch, S., Foster, R. S., & Hankins, T. 1995, *ApJ*, 453, 433
- Manchester, R. N. 1971, *ApJ*, 163, L61+
- Popov, M. V., & Stappers, B. 2007, *A&A*, 470, 1003
- Sallmen, S., Backer, D. C., Hankins, T. H., Moffett, D., & Lundgren, S. 1999, *ApJ*, 517, 460
- Soglasnov, V. A., Popov, M. V., Bartel, N., Cannon, W., Novikov, A. Y., Kondratiev, V. I., & Altunin, V. I. 2004, *ApJ*, 616, 439

Staelin, D. H., & Reifenstein, III, E. C. 1968, Science, 162, 1481